Catal Lett (2009) 129:26–38
DOI 10.1007/s10562-008-9835-4

Replication Route Synthesis of Mesoporous Titanium–Cobalt Oxides and Their Photocatalytic Activity in the Degradation of Methyl Orange

Cheng-Gao Sun · Li Tao · Mei-Lian Fan · Cai-Juan Huang · Eli Ruckenstein · Zi-Sheng Chao

Received: 12 November 2008 / Accepted: 25 December 2008 / Published online: 30 January 2009

Abstract Mesoporous Ti–Co oxides were synthesized via a replication route, using a 3-D wormlike mesoporous silica as template and tetra-tert-butyl orthotitanate (TBOT) and $Co(NO_3)_2$ as source materials. The prepared materials were characterized by X-ray diffraction (XRD), N_2-physisorption, TEM, EDS, and UV/Vis-DRS and found to possess a spherical morphology and a 3-D wormhole-like mesoporous structure, with the average pore size between 4.5 and 16.0 nm. The pore walls consisted mainly of a cobalt-incorporated anatase phase. The Co^{3+} ions were generated in the replicated mesoporous Co–Ti oxides, via the transfer of electrons from Co^{2+} to Ti^{4+} ions. The formation of cobalt-incorporated anatase phase and Co^{3+} ions were both favored by larger Co/Ti atomic ratios and by relatively low calcination temperatures. The specific surface area decreased and the mesopore sizes increased, with increasing Co/Ti atomic ratio or calcination temperature. The average crystal size of the anatase phase decreased with increasing Co/Ti atomic ratio but increased with increasing calcination temperature. The photocatalytic activity of the replicated mesoporous Co–Ti oxides in the degradation of methyl orange dye was investigated. It was observed that the photocatalytic activity increased with increasing Co/Ti atomic ratio and exhibited a maximum with increasing calcination temperature. With the exception of those prepared at too high calcination temperatures, the replicated mesoporous Co–Ti oxides were much more active than the pure titania. It is concluded that, in addition to a higher diffusion, the cobalt-containing anatase, as the active phase, and the Co^{3+} ions, as the active sites, are responsible for the high photocatalytic activity of the replicated mesoporous Co–Ti oxide.

Keywords Mesoporous · Co–Ti oxide · Replication · Photocatalytic degradation · Methyl orange

1 Introduction

Mesoporous materials have high potential for applications in many fields, such as, adsorption/separation, sensors, nano-assemblies, and particularly, catalysis [1–6], due to their high surface area, large pore volume, and regular nano-scale pore size. Much progress has been achieved in the synthesis and application of mesoporous materials, since they were first reported by the Mobil group in 1990s [7, 8]. Several good reviews have been published in the literature [9–11]. Currently, the synthesis of mesoporous materials is mainly based on the sol-gel technology. The controlled hydrolysis of the inorganic precursor species and their subsequent condensation, templated by supramolecular assembly of surfactant micelles, constitute the key steps. The most successful examples are the synthesis of mesoporous silicas, e.g., M41S [7, 8], SAB-n [12, 13], MSU-X [14, 15], and HMS [16]. A few mesoporous metal oxides, such as those of TiO_2, Nb_2O_5, MnO_2, Fe_2O_3 and so on [17–20], and a few mesoporous mixed metal oxides, such as, Ti–M (M = W, V, Fe or Eu) [21–24], V–Mg [25] and Mg–Al [26], were also synthesized. In the sol-gel

C.-G. Sun · L. Tao · M.-L. Fan · C.-J. Huang · Z.-S. Chao (✉)
College of Chemistry and Chemical Engineering, Key Laboratory of Chemometrics & Chemical Biological Sensing Technologies, Ministry of Education, Hunan University, Changsha 410082, China
e-mail: zschao@yahoo.com

E. Ruckenstein (✉)
Department of Chemical and Biological Engineering, State University of New York at Buffalo, Amherst, NY 14268, USA
e-mail: feaeliru@buffalo.edu

synthesis, the hydrolysis of the precursor species has to match their condensation, in order to generate a stable mesoporous phase with all components in the desired proportion and a homogeneous distribution at molecular level. The above requirement is not always easily fulfilled in the synthesis of mesoporous materials, particularly for mixed metal oxides. An alternative approach to the synthesis of mesoporous materials is the replication or the so-called nano-casting technique [27]. It involves the introduction of the precursor species into the pores of a hard template of mesoporous material, followed by the hydrolysis and condensation of precursor species therein, and finally by the removal of the hard template. In this way, the mesoporous materials are manufactured, as negative copies of hard templates. Compared to the sol-gel synthesis of mesoporous materials, the replication method has some advantages. For examples, depending on the hard templates employed, the mesostructures could be directionally fabricated; the elements with a higher hydrolysis capacity but a lower condensation tendency (as is the case with most transition metals) can be employed to manufacture mesoporous materials; the confined space provided by the mesopores of hard template enables effective inclusions of all the components of the mesoporous materials. This is an attractive procedure, because metal oxides have been widely used as catalysts for many organic reactions. In addition, mixed metal oxide catalysts often provide a synergistic effect [28–30], compared with the corresponding single component metal oxides.

Cobalt [31] and titanium [32] usually constitute the key components of the oxidation and photo catalysts and Co–Ti mixed oxides often exhibit enhanced performances as electronic and photo catalysts [33–35]. These materials are all non-porous. Little work was concerned with the synthesis and application of mesoporous Co–Ti oxide catalysts. Previously, we reported about a mesoporous Co–Ti oxide [36] synthesized via the sol-gel route, which exhibited a good performance in the oxidation of cyclohexane to cyclohexanol and cyclohexanone. In the present paper, we are concerned with the synthesis of mesoporous Co–Ti oxides via the replication route, using a 3-D wormhole-like mesostructured silica as hard template. The synthesized mesoporous materials possess a high thermal stability and exhibit a good performance in photocatalytic reactions.

2 Experimental

2.1 Chemicals/Reagents

Tetraethyl orthosilicate (TEOS, A. R., Sinopharm Chemical Reagent Co., Ltds); tetra-tert-butyl orthotitanate (TBOT, Tientsin Fucheng Chemical Cooperation); P25 (A. R., Degussa); NaOH, $Co(NO_3)_2 \cdot 6H_2O$ and ethanol (A. R., Tientsin Damao Chemical Cooperation; $C_{12}H_{25}(OCH_2\text{-}CH_2)_9OH$ (AEO_9), C·P. 99.9 wt%, Nanking Chemical Cooperation); HCl (37 wt%, Changsha Huihong company). Methyl orange (MO, A. R., Sinopharm Chemical Reagent Co., Ltds).

2.2 Synthesis of Mesoporous Silica as a Hard Template

4 g of alkylpolyethyleneoxide ($CH_3(CH_2)_n(OCH_2CH_2)_9$ OH, AEO9) were dissolved in 120 mL of 4 M HCl aqueous solution with stirring at 313 K. After cooling the solution to room temperature, 6 g of tetraethyl orthosilicate (TEOS) were added with stirring. The final mixture was introduced into an autoclave with a Teflon liner and then gelled at 393 K for three days. The solid product was recovered by filtration, washed repeatedly with distilled water and then dried at 373 K for 24 h. The as-synthesized specimen was subjected to thermal treatment at 823 K in air for 6 h to remove the surfactant and then used as hard template in the synthesis of mesoporous Co–Ti oxides.

2.3 Replication Route Synthesis of Mesoporous Co–Ti Oxides, Using Mesoporous Silica as Hard Template

2 g of mesoporous silica template was degassed in a vacuum oven at 373 K for 3 h and then dispersed into 19 mL of an ethanol solution of TBOT (molar ratio TBOT:ethanol = 1:5) at 313 K with vigorous stirring. The resultant mixture was allowed to age statically at 313 K for 10 h, and then 7 mL of a solution, prepared by dissolving 1.74–2.91 g of $Co(NO_3)_2 \cdot 6H_2O$ and 4 g of ethanol into 3 mL of water, was drop-wise added, with vigorous stirring. After addition, the mixture was vigorously stirred at 313 K for another 10 h and turned finally into a green gel with a molar composition of hard template:TBOT:H_2O:ethanol:$Co(NO_3)_2$ = 1:1:5:10:.18–0.3 (the mole of hard template was calculated on the basis of SiO_2). The gel was dried at 373 K for 24 h, washed repeatedly with deionized water, and then calcined in air at a temperature ranging from 773 to 1,123 K for 4 h, thus resulting a Co–Ti–Si–O composite. To remove the hard template, the composite was dispersed in a 5 wt% NaOH aqueous solution, with a weight ratio of solid:liquid = 1:40, and heated at 333 K for 24 h, with stirring. Otherwise mentioned specially, the above NaOH treatment was repeated again. The solid specimen was recovered by filtration, washed with deionized water, and dried at 373 K, resulting in the mesoporous Ti–Co oxide. The materials prepared via the above procedure is denoted as Co–Ti–O(T–R), where T indicates the calcination temperature used to generate the Co–Ti–Si–O

composite and R indicates the Co/Ti atomic ratio in the initial batch.

2.4 Characterization of the Replicated Mesoporous Co–Ti Oxides

X-ray diffraction (XRD) was performed using a Brucker D8 advance diffractometer (Cu Kα radiation, wavelength 1.5406 Å; 40 kV and 40 mA). The diffractometer was operated in a 2θ mode and the diffraction pattern was scanned at a speed of 0.02°/sec.

Nitrogen adsorption-desorption was performed at 77 K using a Beckman Counter SA-3100 gas sorption and porosimetry instrument. Before the adsorption measurements, the specimen was heated from room temperature up to 573 K, evacuated to 10^{-3} Pa, and then kept at that temperature and vacuum for outgasing for 2 h. The specific surface area was determined by the BET method and the pore size distribution was obtained from the N_2-desorption branch by the BJH (Barrett–Joyner–Halenda) method.

High resolution transmission electron microscopy (HR-TEM) was carried out using a JEM-3010 field emitting electron microscope, operated at 300 kV accelerating voltage. Energy dispersive X-ray spectroscopy (EDS) was performed using an elemental analysis accessory (Oxford) of the JEM-3010 instrument.

Ultraviolet-visible diffuse reflection (UV/Vis-DRS) spectroscopy was carried out using a Perkin Elmer Lambda 35 UV-vis spectrometer. The data have been collected between 200 and 800 nm using $BaSO_4$ as reference.

2.5 Photo Degradation of Methyl Orange Dye Over the Replicated Mesoporous Co–Ti Oxide Catalysts

The photocatalytic activity of the replicated macro-mesoporous Co–Ti oxides was investigated by examining the photo degradation of methyl orange dye (MO, commercial source, analytical reagent) in water at room temperature. For comparison purpose, the photocatalytic activity over the commercial Degussa P25, i.e., pure titania, was also examined. The UV photocatalytic degradation of MO was carried out in a quartz reactor, using a radiation source of 300 W high-pressure mercury lamp with a wavelength centered at 365 nm. In a typical run, a 50 mg catalyst powder was first homogeneously dispersed in 60 mL of MO aqueous solution with a concentration of 30 mg/L and then subjected to UV illumination, with magnetic stirring. The sunlight photocatalytic degradation of MO was performed in a sealed glass beaker. To each of a group of 250 mL beakers, 100 mL of MO aqueous solution with a concentration of 80 mg/L was added, and then 50 mg catalyst powder was dispersed with stirring. The beakers were sealed and placed statically in the outdoor environment. In both, UV and sunlight photocatalytic degradation of MO, samples were taken from the reactor or beaker at regular intervals. The samples were centrifuged to remove the catalyst and then the concentration of MO was determined. The analysis was performed on a Perkin Elmer Lambda 35 UV-Vis spectrometer at 465 nm wavelength.

3 Result and Discussion

3.1 Structural and Textural Properties

Figure 1 shows the low-angle XRD spectra of the hard template, Co–Ti–Si–O composite and replicated Co–Ti oxide for a molar ratio of Co:Ti = 0.24:1. A broad peak at $2\theta = 0.9^{o}$ (d = 9.7 nm) was present in the XRD spectrum of the hard template (Fig. 1a). When the hard template was incorporated with Ti and Co sources, then dried at 373 K for 24 h, and finally calcined at 773 K for 4 h, thus generating the Ti–Co–Si–O composite, the broad peak disappeared (Fig. 1b). This occurred because mesopors of the hard template was fulfilled by the Ti and Co species [37]. After the composite was treated once with NaOH, almost no peak could be detected in the XRD spectrum (Fig. 1c), indicating that most of the mesopores were still filled with Ti and Co species. However, after the composite was treated twice with NaOH, generating Co–Ti–O(773-

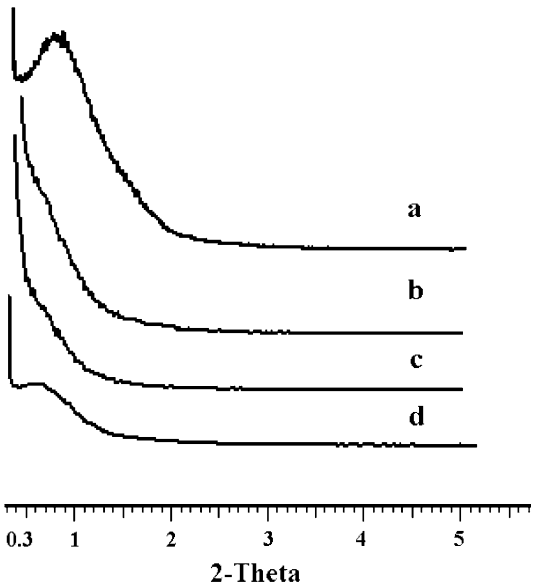

Fig. 1 Low angle Powder X-ray diffraction patterns of the hard template and Co–Ti–Si–O composite as well as of the replicated Co–Ti oxide with an atomic ratio of Co:Ti = 0.24:1. (a) hard template; (b) Co–Ti–Si–O composite; (c) and (d), replicated Co–Ti oxide, prepared by treating the Co–Ti–Si–O composite with a NaOH solution for 24 h once and twice, respectively

0.24), the broad peak appeared again, with its diffraction angle shifted to $2\theta = 0.621^{o}$ (d = 14.21 nm) (Fig. 1d). The broad peak in the low angle range of XRD spectrum indicates the presence of a 3-D wormhole-like mesophase, as observed generally in mesoporous silica and titania [15, 38, 39]. The above results indicate that a mesoporous Co–Ti oxide has been synthesized via the replication route.

Wide angle XRD spectra of the Co–Ti–Si–O composite and replicated Co–Ti oxide for an atomic ratio of Co:Ti = 0.24:1, are presented in Fig. 2. No peak was detected in the wide angle XRD spectrum of the hard template (not introduced in the paper), indicating an amorphous nature of the pore wall of the hard template. When the hard template was first impregnated with Ti and Co sources and then dried at 373 K for 24 h, no peak occurred in the XRD spectrum (Fig. 2a). After the specimen was calcined at 773 K for 4 h, generating the Ti–Co–Si–O composite, five broad peaks (2θ = 25.3, 37.9, 48.1, 53.9, and 55.6°), corresponding to the (101), (103), (004), (105) and (211) planes of the anatase phase, and a few weak peaks, belonging to the rutile phase, could be observed (Fig. 2b). No other phases, such as Co_xO_y or $Co_xTi_yO_z$, had been identified, suggesting that the cobalt ions have been incorporated into the framework of titania. It can be evaluated from the diffraction pattern that the titania in the Ti–Co–Si–O composite consists of about 89.7% of anatase and about 10.3% of rutile. Using Scherrer equation, the crystal size of the anatase phase was evaluated to be about 6–8 nm. After the specimen was treated with NaOH solution once and twice (the Co–Ti–O(773-0.24)), no obvious change could be identified in the XRD spectra (Fig. 2c, d).

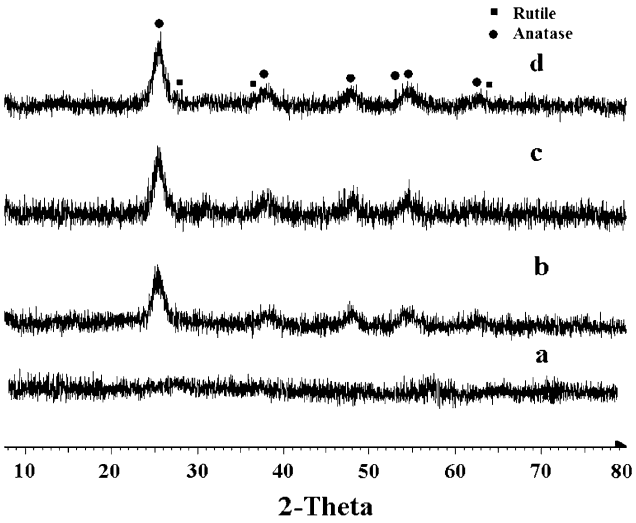

Fig. 2 Wide angle powder X-ray diffraction patterns of the hard template and Co–Ti–Si–O composite as well as the replicated Co–Ti oxide with an atomic ratio of Co:Ti = 0.24:1. (a) and (b), Co–Ti–Si–O composite, before and after a calcination at 773 K; (c) and (d), the replicated Co–Ti oxide, prepared by treating the Co–Ti–Si–O composite, after (b), with NaOH solution for 24 h for once and twice, respectively

Figure 3 presents the low angle XRD spectra of the Co–Ti–O(773-R) specimens. Wide peaks are present in the spectra of the specimens, similar to that in Fig. 1d. It indicates that the specimens possess a 3-D wormhole-like mesostructures. The d-spacings of these peaks are listed in Table 1 and shown to increase with increasing Co/Ti atomic ratio.

Figure 4 presents the wide angle XRD spectra of commercial P25 titania and Co–Ti–O(773-R) specimens. As well known, P25 consists of ca. 80% anatase and 20% rutile. In Co–Ti–O(773-R), both anatase and rutile phases are present, and the content of the rutile phase decreased

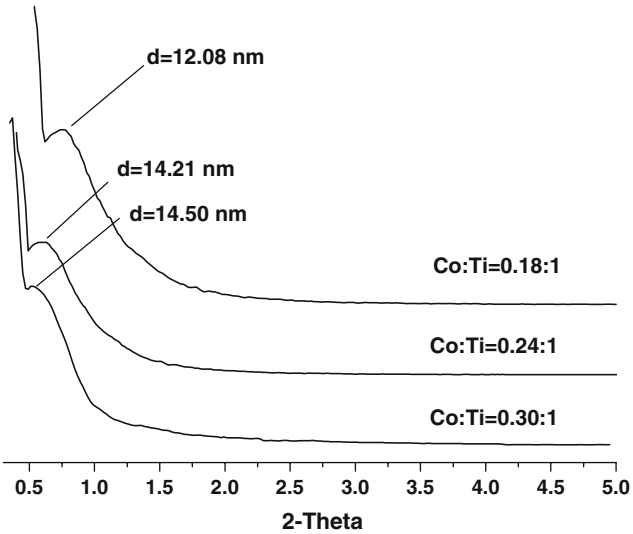

Fig. 3 Low angle XRD spectra of the Co–Ti–O(773-R) specimens

Table 1 Textural property of the hard template and Co–Ti–O(773-R) specimens

Specimen	*d-spacing* (nm)	S_{BET} (m^2/g)	D_p (nm)	D_w (nm)	V_p (cc/g)
Hard template	9.70	680.94	6.67	3.03	1.36
Ti–Co–O(773-0.18)	12.08	154.65	4.63	7.45	0.21
Ti–Co–O(773-0.24)	14.21	92.21	6.89	7.32	0.15
Ti–Co–O(773-0.30)	14.50	68.49	7.33	7.07	0.07

Note: S_{BET} specific surface area, D_p pore size, D_w thickness of the pore wall, obtained by subtracting D_p from *d-spacing*, V_p pore volume

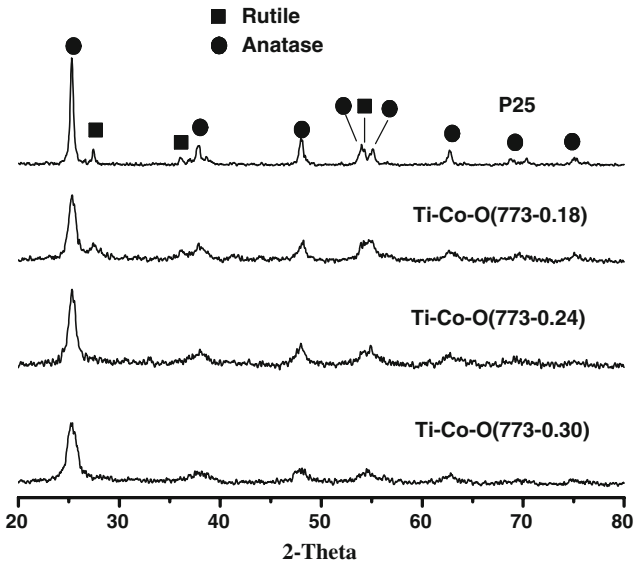

Fig. 4 Wide angle XRD spectra of the Co–Ti–O(773-R) specimens

with increasing Co/Ti atomic ratio. This result suggests that the cobalt ions are incorporated into the lattice of the rutile phase. Because rutile has a higher symmetry than anatase, the incorporation of cobalt ions into the lattice of rutile reduces the symmetry of titania, resulting in the transformation of rutile to anatase. It can be expected that the anatase lattice has only a limited accommodation for cobalt ions, and with the increase of Co/Ti atomic ratio, the anatase crystals would split into smaller ones. The average crystal size of the anatase phase in the Co–Ti–O(773-R) specimens has been calculated using the Scherrer equation, on the basis of the (101) and (200) planes. The results are listed in Table 2 and show indeed that with increasing Co/Ti atomic ratio, the average crystal size decreases.

Figure 5 presents the N_2-physorption isotherm and the pore size distribution curve for the hard template. One can see that the adsorption-desorption isotherm belongs to type IV, and this indicates the presence of a mesophase [40, 41]. The hysteresis loop of the isotherm starts at $P/P_0 = 0.38$ and is very close to type H1, suggesting that the mesopores of the template have an open cylindrical shape and the pore size is narrowly distributed [41]. Evidence for a narrow pore size distribution of the template is also provided by the curve in the inset of Fig. 5.

Figure 6 presents the N_2-physorption isotherms and pore size distribution curves of the Co–Ti–O(773-R) specimens. All isotherms are of type IV and the hysteresis loops are close to type H2 (Fig. 6a), indicating that the mesopores in the specimens possess a complex shape, e.g., ink bottle or narrow-mouth sphere [42]. The adsorption capacity decreased with increasing Co/Ti atomic ratio, indicating a reduction in porosity and specific surface area. The hysteresis loops started at $P/P_o = 0.37$, 0.39 and 0.41 for the replicated mesoporous Co–Ti oxides with atomic ratios of Co:Ti = 0.18, 0.24 and 0.3, respectively. This indicates an increase in the mesopore size with increasing Co/Ti atomic ratio, because the higher the starting value P/P_o of the hysteresis loop is, the larger the pore size of the mesoporous material would be [42]. The BJH pore size distribution curves of the Co–Ti–O(773-R) specimens (Fig. 6b) show that the pore size distributions became

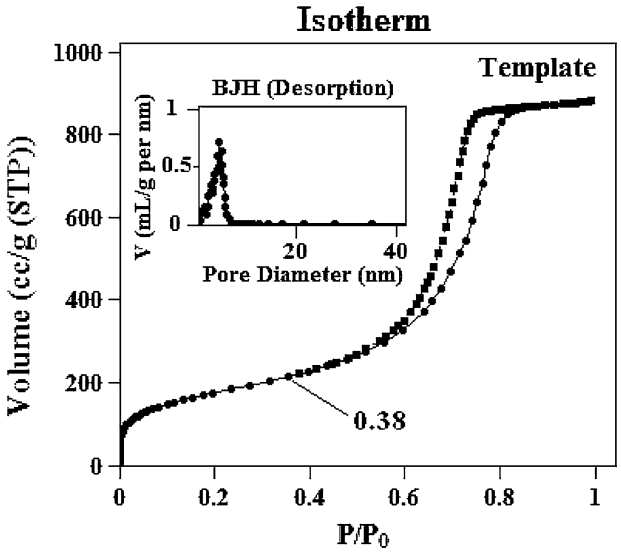

Fig. 5 N_2 adsorption/desorption isotherm and BJH pore size distribution of the hard template

Table 2 Crystallite sizes of the anatase phase in Co–Ti–O(T–R) specimens calculated with the Scherrer formula, on the basis of the (101) and (200) planes

Specimens	C_{101}/C_{200} (nm)	Specimens	C_{101}/C_{200} (nm)	Specimens	C_{101}/C_{200} (nm)
Ti–Co–O(773-018)	10.2/11.5	Ti–Co–O(773-024)	9.3/7.2	Ti–Co–O(773-0.3)	8.6/6.1
Ti–Co–O(923-0.18)	43.2/19.6	Ti–Co–O(923-0.24)	38.7/21.3	Ti–Co–O(923-0.3)	29.4/16.0
Ti–Co–O(1023-0.18)	N. A.*	Ti–Co–O(1023-0.24)	N. A.	Ti–Co–O(1023-0.3)	>1,000**
Ti–Co–O(1123-0.18)	N. A.	Ti–Co–O(1123-0.24)	N. A.	Ti–Co–O(1123-0.3)	N. A.

* Scherrer equation is inapplicable to the evaluation of crystal size, due to the small FWHM of the diffraction peaks, indicating a crystal size larger than 100 nm

** No anatase phase was identified by XRD

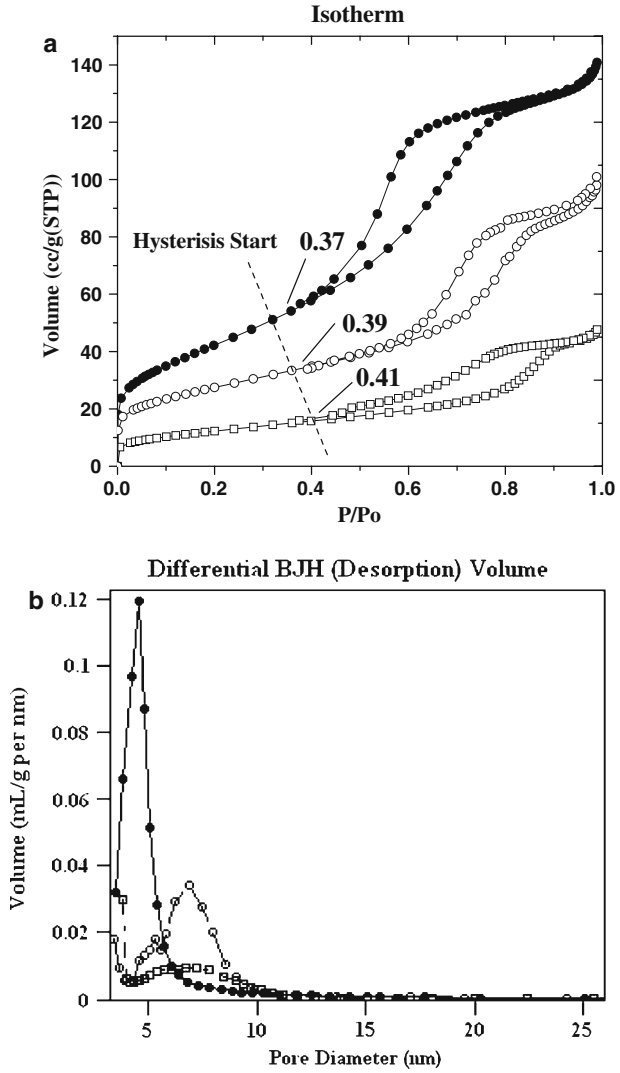

Fig. 6 **a** N_2 adsorption/desorption isotherm; **b** BJH pore size distribution of the Co–Ti–O(773-R) specimens. (Legends: ● Co–Ti–O(773–0.18); ○ Co–Ti–O(773–0.24); □ Co–Ti–O(773–0.3))

wider and the pore size increased, with increasing Co/Ti atomic ratio.

The textural properties, identified by XRD and N_2-physisorption, of the hard template and Co–Ti–O(773-R) specimens are summarized in Table 1. One can see that the specific surface area and pore volume of the Co–Ti–O(773-0.18) are smaller than those of the hard template. This occurs because the hard template is of high porosity and the replicated mesoporous Co–Ti oxide is a negative copy of the hard template. The d-spacing of Co–Ti–O(773-0.18) is larger than that of the hard template. This might be a result of the swelling of the pore wall of the hard template, in the presence of water and the dissociation of the polysilicate, during the removal of the hard template from the Co–Ti–Si–O composite by NaOH. The fact that the pore size of the Co–Ti–O(773-0.18) is larger than the thickness of the pore wall of the hard template provides additional evidence for the above conclusion. The thickness of pore wall of Co–Ti–O(773-0.18) is found to be larger than the pore size of the hard template. This might occur because the pore wall of the hard template is partially soaked by the Co and Ti sources, during the formation of Co–Ti–Si–O composite. From Table 1, one can also see that for Co–Ti–O(773-R), the BET specific surface area, pore volume and thickness of pore wall decreased whereas the d-spacing and pore size increased, with increasing Co/Ti atomic ratio. This probably occurs because a fraction of the anatase crystals were "extracted" from the pore wall of Co–Ti–O(773-R), during the removal of the hard template by NaOH, resulting in the partial collapse of the mesostructure of Co–Ti–O(773-R). As mentioned in the discussion regarding Fig. 3, with increasing Co/Ti atomic ratio, the anatase crystals were split into smaller ones. The smaller the anatase crystal is, the larger tendency the anatase crystal would exhibit to be extracted from the pore wall. Therefore, with increasing Co/Ti atomic ratio, the porosity of Co–Ti–O(773-R) decreases and the thickness of the pore wall becomes thinner.

TEM micrographs of the hard template and Co–Ti–O(773-0.24) specimen are presented in Fig. 7. This figure shows that the hard template has a typical 3-D wormhole-like mesostructure (Fig. 7a). The replicated mesoporous Co–Ti oxide exhibits a regular spherical morphology (Fig. 7b), with a diameter ranging from about 50 to about 250 nm, and possesses a 3-D wormhole-like mesostructure (Fig. 7c), similar to that of the hard template. The HR-TEM micrograph (Fig. 7d) indicates the presence of well-resolved lattice fringes, which demonstrates that the pore walls of the mesopores are composed mainly of anatase nanocrystals with a size of about 5–10 nm. This result is consistent with that calculated from the XRD experiments using the Scherrer equation.

The EDS spectra of the Co–Ti–O(773-R) specimens are presented in Fig 8. No silica was found in the EDS spectra, indicating the complete removal of the hard template during the NaOH treatment. The atomic ratios of Ti/Co in the replicated mesoporous Co–Ti oxides, determined by EDS, are 1:0.17, 1:0.22 and 1:0.28, respectively, values which are approximately the same as those of the initial batches, i.e., 1:0.18, 1:0.24 and 1:0.3.

The UV/Vis-DRS spectra of the commercial P25 (pure titania) and Co–Ti–O(773-R) specimens are presented in Fig. 9. In the UV range, the spectrum of the pure TiO_2 exhibits a strong absorption, caused by the interband transition from the valence to the conduction band. Two broad bands, centered at about 230 and 330 nm, could be identified (Fig. 9a), due to the charge transfer (C–T) of O^{2-} to Ti^{4+} [43]. Over the replicated mesoporous Co–Ti oxide, the absorptions are stronger than over the pure titania and

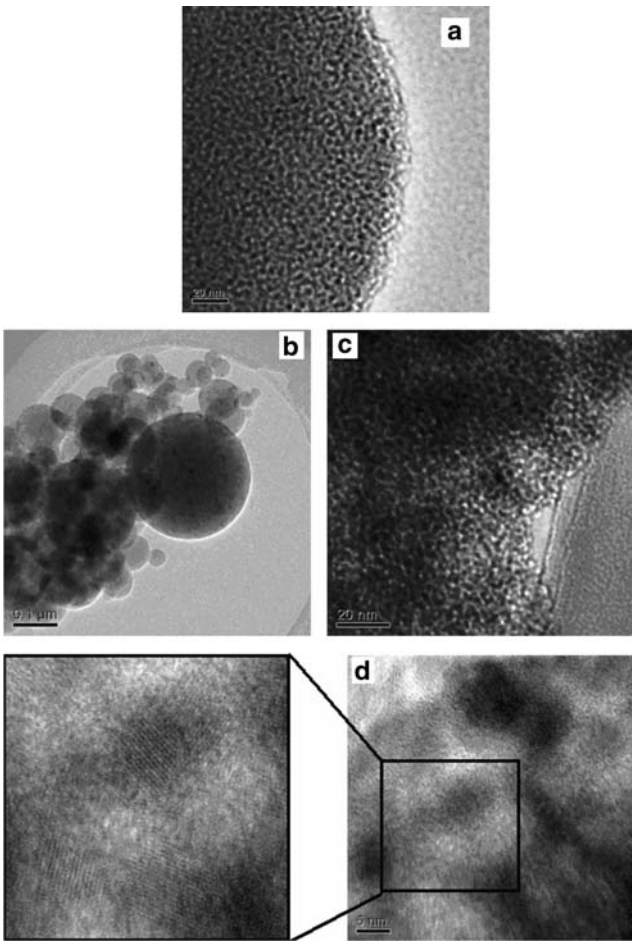

Fig. 7 TEM micrographs of the hard template and Co–Ti–O(773–0.24) specimen. **a** hard template; **b–d**, Co–Ti–O(773-0.24), with increasing the magnification of micrograph

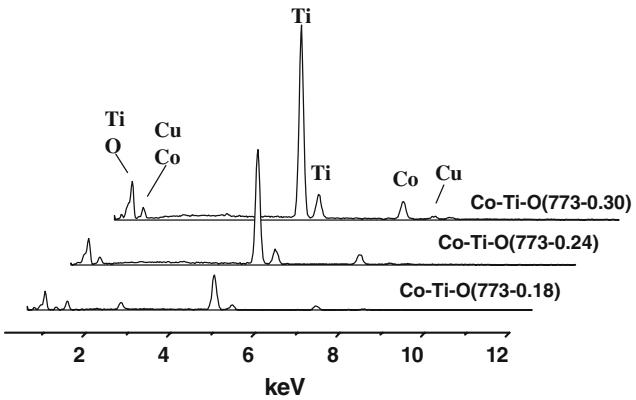

Fig. 8 EDS patterns of the Co–Ti–O(773-R) specimens. (a) Co–Ti–O(773-0.18); (b) Co–Ti–O(773-0.24); (c) Co–Ti–O(773-0.3)

increase with increasing Co/Ti atomic ratio (Fig. 9b–d). The absorption edges of the replicated mesoporous Co–Ti oxides are extended into the visible light range, whereas that for pure titania is limited at 400 nm. Three absorption

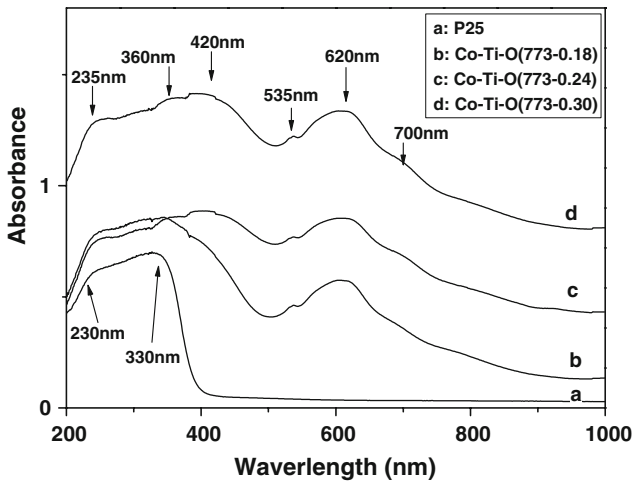

Fig. 9 UV/Vis-DRS spectra of Co–Ti–O(773-R). (a) pure TiO_2 (P25); (b) Co–Ti–O(773-0.18); (c) Co–Ti–O(773-0.24); (d). Co–Ti–O(773-0.3)

bands at about 235, 330 and 360 nm could be identified over the replicated mesoporous Co–Ti oxide. These results suggest that the cobalt species have been incorporated into the framework of titania, resulting in the splitting of the titania lattice into many small entities, and accordingly, the bending of energy band in titania [44]. In the visible light range, several bands, centered at about 420, 535, 570, 620, 700 and 780 nm, could be identified over the replicated Co–Ti oxide, in contrast to none over the pure titania. In the visible light range, cobalt species of different valences and coordinations usually exhibit a spectrum with multiple absorptions, which are not easy to distinguish between each other, due to the partial overlap of the absorptions. Table 2 in ref. [43] summarized the adsorptions and their assignments over various cobalt-containing compounds. On the basis of that table, the absorptions at 420 and 700 nm over the replicated mesoporous Co–Ti oxides can be assigned to the $^1A_{1g} \rightarrow {}^1T_{2g}$ and $^1A_{1g} \rightarrow {}^1T_{1g}$ transitions of Co^{3+} ions in the octahedral symmetry, those at 535 and 780 nm to the $^4T_{1g} \rightarrow {}^4T_{1g}(P)$ and $^4T_{1g} \rightarrow {}^4A_{2g}$ (F) transitions of Co^{2+} ions in the octahedral symmetry, and those at 570 and 620 nm to the $^4A_2 \rightarrow {}^4T_1(P)$ transition of Co^{2+} ions in the tetrahedral symmetry. The absorption at 420 nm can also be ascribed to the $Co^{2+} \rightarrow Ti^{4+}$ intervalence charge transition [43]. The above results suggest that the cobalt species, Co^{2+} and/or Co^{3+}, are incorporated into the framework of titania in the replicated mesoporous Co–Ti oxide. The presence of Co^{3+} ions is probably due to the oxidation of a part of Co^{2+} ions during the calcination step of preparing the replicated mesoporous Co–Ti oxide. It is also possible that, when Co^{2+} ions are incorporated into the framework of titania (Ti^{4+}), excess negative charges are introduced around the lattice points occupied by the Co^{2+} ions. To maintain neutrality of the lattice, the Co^{2+} ions have to

transfer electrons to Ti^{4+}, via the Co-O–Ti bridge bond, thus generating Co^{3+} ions. The electron transfer from the Co^{2+} to Ti^{4+} ions is promoted by UV/Vis illumination, as evidenced by the band at 420 nm in the UV/Vis-DRS spectra of replicated mesoporous Co–Ti oxide. The UV/Vis-DRS spectroscopic characteristics of the replicated mesoporous Co–Ti oxide, e.g., the higher absorptions than over pure titania, the presence of absorptions in the visible light range, and the formation of Co^{3+} ions, suggest that they possess photocatalytic and oxidation catalytic capabilities [44–50].

The effect of calcination temperature of the Co–Ti–Si–O composite during the preparation of Co–Ti–O(T-0.24) were examined by XRD and the results are presented in Fig. 10. In the low angle XRD spectra (Fig. 10a), the Co–Ti–O(773-0.24) and Co–Ti(923-0.24) specimens displayed a XRD peak, which indicates the presence of a mesostructure. However, the peak intensity of Co–Ti(923-0.24) was much lower than that of Co–Ti(773-0.24). No obvious peak was detected over the Co–Ti–O(1023-0.24) and Co–Ti–O(1123-0.24) specimens. This suggests that the mesostructure collapsed partially at high temperatures. In the wide-angle range of XRD spectra (Fig. 10b), the anatase was identified as the only phase present in the Co–Ti–O(773-0.24) specimen. With increasing calcination temperature to 923 K, the diffraction peaks for the anatase phase decreased in intensity and those of the rutile phase appeared in the XRD spectrum of the Co–Ti–O(923-0.24) specimen. By further increasing the calcination temperature to above 923 K, for Co–Ti–O(1023-0.24) and Co–Ti–O(1123-0.24), the characteristic XRD peaks of $CoTiO_3$ appeared, while those of anatase disappeared and those of rutile increased in intensity. The above results indicate that the anatase identified in the replicated mesoporous Co–Ti oxide is incorporated with cobalt ions. A transfer of cobalt ions probably occurs between the entities of the anatase phase, similar to a disproportion reaction, and promoted by high calcination temperatures. This results in an anatase phase with high atomic ratio of Co/Ti and a rutile phase with an atomic ratio of Co/Ti = 0. Even though we did not determine the increase of Co/Ti atomic ratio with increasing calcination temperature, the atomic ratio of Co/Ti = 1 in the $CoTiO_3$ identified at a calcination temperature of 1023 K provides some evidence in this direction. From Fig. 10, one can see that the diffraction peaks for Co–Ti–O(773-0.24) and Co–Ti–O(923-0.24) are remarkably wider than for Co–Ti–O(1023-0.24) and Co–Ti–O(1123-0.24). It indicates that the average crystal size for the former two specimens is smaller than the later two specimens. Using the planes (101) and (200) of the anatase phase as a basis, the average crystal sizes of Co–Ti–O(773-0.24) and Co–Ti–O(923-0.24) were calculated with the Scherrer equation, and the results are listed in Table 2,

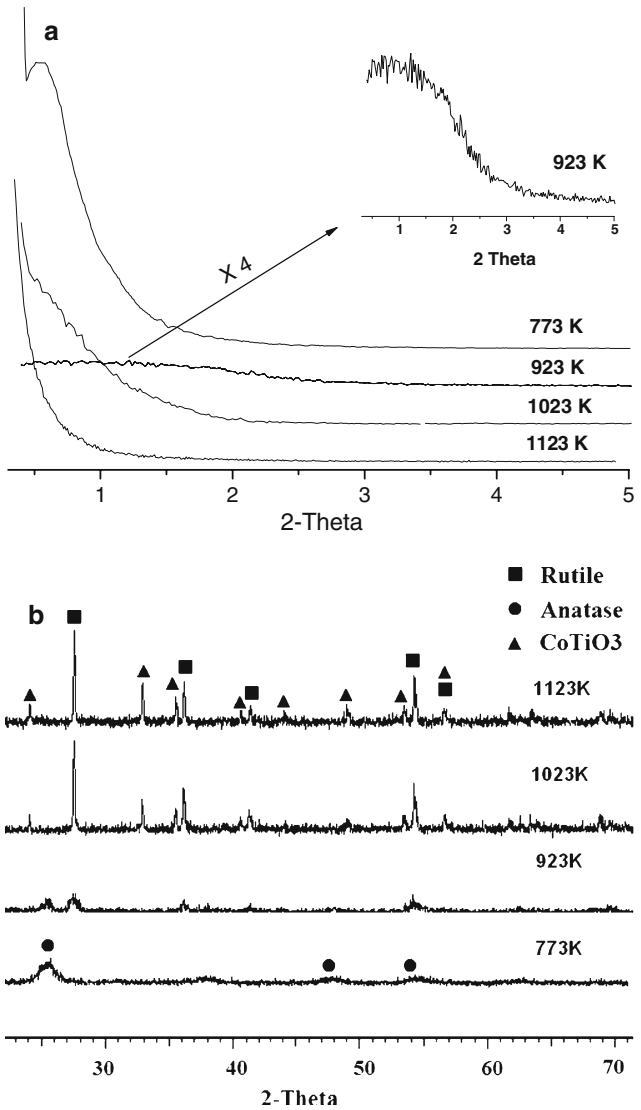

Fig. 10 Low angle **a** and wide angle **b** XRD patterns of the Co–Ti–O(T-0.24) specimens (Inset: the XRD pattern of Co–Ti–O(923-0.24) was enlarged in *y*-axis direction)

which shows that Co–Ti–O(923-0.24) has a larger average crystal size than Co–Ti–O(773-0.24). The diffraction peaks for Co–Ti–O(1023-0.24) and Co–Ti–O(1123-0.24) have so small FWHMs (full width at half maximum) of the diffraction peaks that they are inapplicable to calculate the crystal size with the Scherrer equation, indicating that the average crystal sizes for these specimens are larger than 100 nm. The above results indicate that, with increasing calcination temperature, anatase was transformed into rutile and $CoTiO_3$ phases, accompanied by an increase in the average crystal size.

Figure 11 presents the N_2-physisorption isotherms (Fig. 11a) and pore size distribution curves (Fig. 11b) of Co–Ti–O(T-0.24). One can see that the isotherms of Co–Ti–O(773-0.24), Co–Ti–O(923-0.24) and Co–Ti–

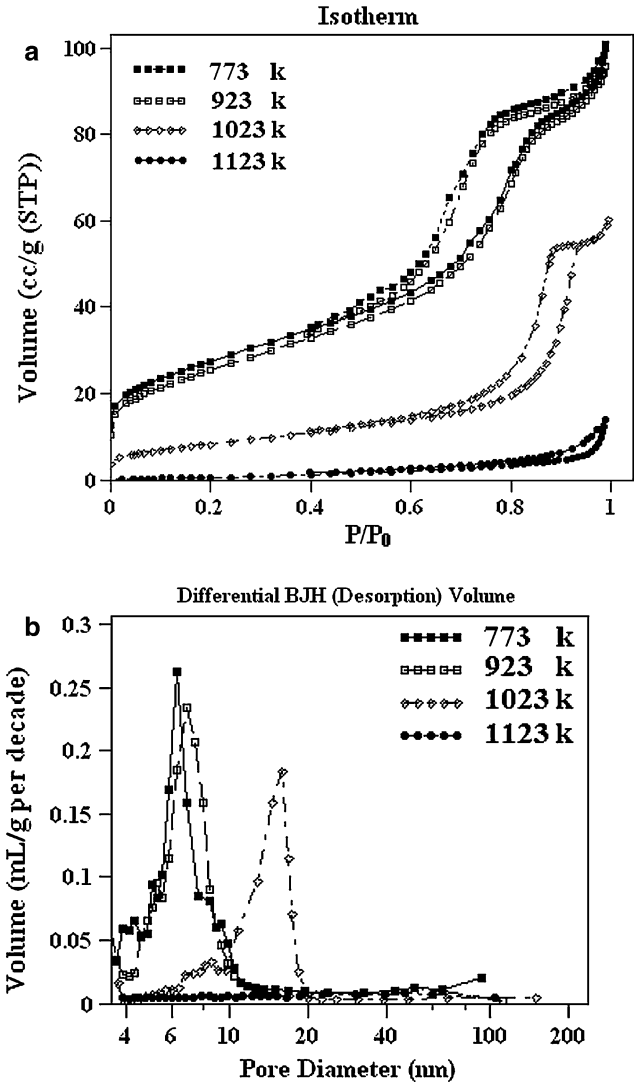

Fig. 11 **a** N_2 adsorption/desorption isotherms; **b** BJH pore size distributions of Co–Ti–O(T-0.24)

O(1023-0.24) are all of type IV and that the hysteresis loops are close to type H2, indicating that the mesopores in the specimens possess a complex shape, such as, the ink bottle or the narrow-mouth sphere [42]. The adsorption capacity over these specimens decreased, however, with increasing calcination temperature, revealing a decrease in porosity. For Co–Ti–O(1123-0.24), the isotherm and hysteresis loop are of types IIb and H3 and the adsorption capacity is much smaller than those for Co–Ti–O (R-0.24) prepared at lower calcination temperatures. This indicates a non-porous or macroporous nature of Co–Ti–O(1123-0.24). From the pore size distribution curves, one can see that, for Co–Ti–O(T-0.24), the pore size increases with increasing calcination temperature and that Co–Ti–O(1123-0.24) has a much more wide pore size distribution than the other specimens. The effect of calcination temperature on the textural properties of the replicated

Table 3 BET specific surface area (S_{BET}), BJH pore size and pore volume (Vp) of the template and the Co–Ti–O(T-0.24) specimens

Specimen	S_{BET} (m^2/g)	D_p (nm)	V_p (cc/g)
Ti–Co–O(773-0.24)	92.21	6.69	0.146
Ti–Co–O(923-0.24)	85.86	7.31	0.133
Ti–Co–O(1023-0.24)	30.33	15.92	0.089
Ti–Co–O(1123-0.24)	5.47	34.5*	0.002

Note: S_{BET} specific surface area, D_p pore size, V_p pore volume

* Average BJH pore size

mesoporous Co–Ti oxide is provided by the data in Table 3. It shows that, with increasing calcination temperature, the BET specific surface area and pore volume decreased and the pore size increased. This probably occurs because the mesoporous structure collapsed at higher calcination temperatures.

The UV/Vis-DRS spectra of P25 and Co–Ti–O(T-0.24) are presented in Fig. 12. In the UV range, the absorptions are stronger for Co–Ti–O(773-0.24), Co–Ti–O(923-0.24) and Co–Ti–O(1023-0.24) and lower for Co–Ti–O(1123-0.24) than for the pure titania. In addition, the C–T band at 240 nm for the pure titania is blue-shifted by 28, 31 and 22 nm for Co–Ti–O(773-0.24), Co–Ti–O(923-0.24) and Co–Ti–O(1023-0.24), respectively. However, a blue shift was not observed for Co–Ti–O(1123-0.24). The blue shift of the C–T band usually indicates a higher photocatalytic activity [49]. In contrast to a band edge at about 400 nm for the pure titania, the band edge of the replicated mesoporous Co–Ti oxide is extended into the range of visible light absorption. As in Fig. 9, bands at about 420, 535, 570, 620, 700 and 780 nm can be identified for Co–Ti–O(T-0.24). The bands at 420 and 700 nm can be assigned to the $^1A_{1g} \rightarrow {}^1T_{2g}$ and $^1A_{1g} \rightarrow {}^1T_{1g}$ transitions of Co^{3+} ions in the octahedral symmetry, those at 535 and 780 nm to the $^4T_{1g} \rightarrow {}^4T_{1g}$(P) and $^4T_{1g} \rightarrow {}^4A_{2g}$ (F) transitions of Co^{2+}

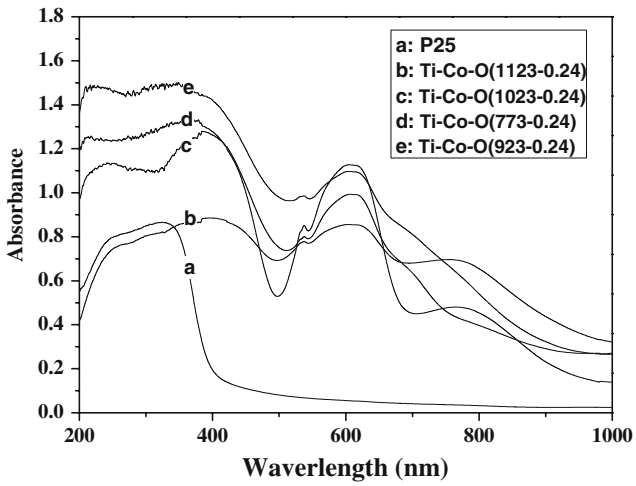

Fig. 12 UV/Vis-DRS spectra of P25 and Co–Ti–O(T-0.24)

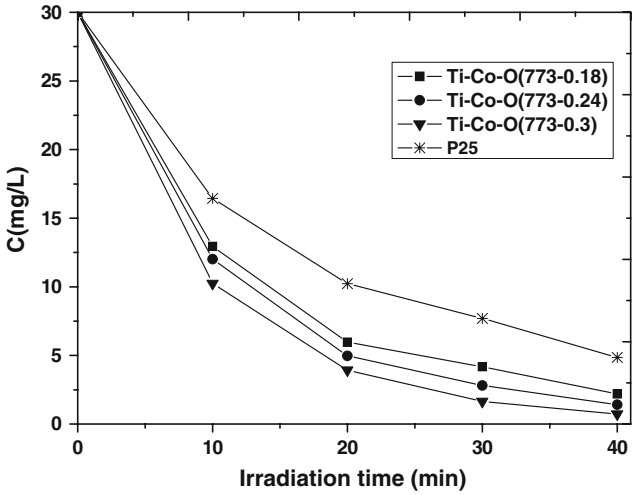

Fig. 13 Kinetic curves for the UV photo degradation of MO aqueous solutions over P25 and Co–Ti–O(773-R)

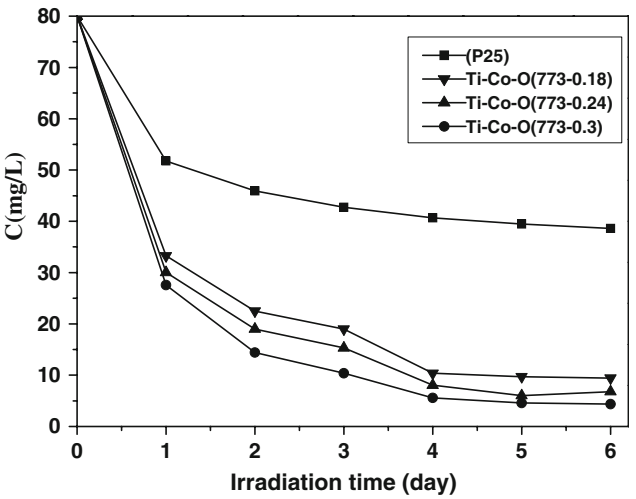

Fig. 14 Kinetic curves for the sunlight photocatalytic degradation of MO over P25 and Co–Ti–O(773-R)

ions in the octahedral symmetry, and those at 570 and 620 nm to the $^4A_2 \rightarrow {}^4T_1(P)$ transition of Co^{2+} ions in the tetrahedral symmetry [43]. The band at 420 nm can be also assigned to the $Co^{2+} \rightarrow Ti^{4+}$ intervalence charge transition [51]. Comparing Co–Ti–O(1023-0.24) and Co–Ti–O(1123-0.24) to Co–Ti–O(773-0.24) and Co–Ti–O(923-0.24), the intensity of the band at about 700 nm ($^1A_{1g} \rightarrow {}^1T_{1g}$ transitions of Co^{3+} ions in octahedral symmetry) is reduced but that at 780 nm ($^4T_{1g} \rightarrow {}^4A_{2g}$ (F) transitions of Co^{2+} ions in the octahedral symmetry) is increased. One can conclude that the presence of Co^{3+} ions is not due mainly to the oxidation of Co^{2+} during the calcination step but to an electron transfer from Co^{2+} to Ti^{4+}, as pointed out in the discussion regarding Fig. 9. At higher temperatures (>923 K), the reaction between cobalt ions with titania transforms the cobalt-containing anatase into rutile and $CoTiO_3$ (see Fig. 10), and, as a result, the band at 700 nm is decreased and that at 780 nm is increased.

3.2 Activity for Photocatalytic Degradation of Methyl Orange (MO)

Figure 13 presents the kinetic curves for the UV light photocatalytic degradation of methyl orange (MO) over P25 and Co–Ti–O(773-R) catalysts. One can see that, with increasing illumination time, the MO concentration decreases rapidly over all catalysts tested. The UV photocatalytic activity over Co–Ti–O(773-R) catalysts are significantly higher than over P25 and increases with the Co/Ti atomic ratio. For an illumination time of 40 min, the MO concentration decreases from the original 30 mg/L to 1.27, 1.85, 3.00 and 5.41 mg/L, corresponding to a MO conversion of 95.77, 98.33, 90.00 and 81.97%, over the Co–Ti–O(773-R) catalysts with atomic ratios of Co/Ti = 0.3, 0.24 and 0.18 and the P25 catalysts, respectively.

Figure 14 presents the kinetic curves for the sunlight photocatalytic degradation of MO over P25 and Co–Ti–O(773-R) catalysts. One can see that, for an illumination time of 1 day, the MO concentration decreases from 80 mg/L to 51.78 mg/L over P25 and to 33.26, 30.01 and 25.57 mg/L over Co–Ti–O(773-R) with an atomic ratio of Co/Ti = 0.18, 0.24 and 0.30, respectively. With prolonged illumination times, the MO concentration decreases slowly over P25 catalyst and rapidly over Co–Ti–O(773-R) catalysts. For example, for an illumination time of 4 days, the MO concentration decreased to 40.66 mg/L over P25 and to 10.39, 8.03 and 5.55 mg/L over the Co–Ti–O(773-R) with atomic ratios of Co/Ti = 0.18, 0.24 and 0.30, respectively. For illumination times longer than 4 days, the rate of photocatalytic degradation of MO over all catalysts becomes slower. For example, for a radiation time of 6 days, the MO concentration decreases to 38.63, 9.43, 6.78 and 4.36 mg/L, corresponding to a MO conversion of 51.71, 88.21, 91.53 and 94.55%, over P25 and Co–Ti–O(773-R) with atomic ratios of Co/Ti = 0.18, 0.24 and 0.30, respectively. This reveals that the activity of the photocatalytic degradation of MO over the replicated mesoporous Co–Ti oxide catalysts is lager than over P25 and increases with the Co/Ti atomic ratio.

Figure 15 presents the kinetic curves for the UV photocatalytic degradation of MO over P25 and Co–Ti–O(T-0.24) catalysts. One can see that by prolonging the illumination time, the MO concentration decreases over all catalysts. The activity of photocatalytic degradation of MO occurs in the sequence Co–Ti(923-0.24) > CoTi(773-0.24) > Co–Ti(1023-0.24) > P25 > Co–Ti(1123-0.24). For an illumination time of 40 min, the MO concentration decreases from the original 30 mg/L to 0.04, 1.57, 2.97, 4.85 and 9.6, corresponding to a MO conversion of 99.87,

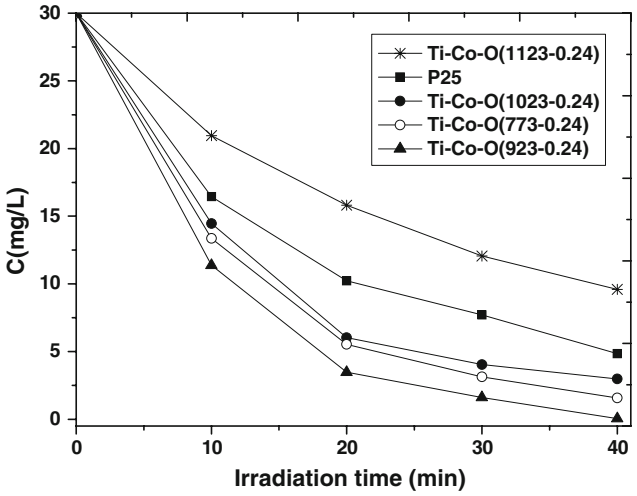

Fig. 15 Kinetic curves of the UV photo degradation of MO aqueous solutions over P25 and Co–Ti–O(T-0.24)

94.77, 90.10, 83.83 and 68.00% over Co–Ti(923-0.24), CoTi(773-0.24), Co–Ti(1023-0.24), P25 and Co–Ti(1123-0.24), respectively.

Figure 16 presents the kinetic curves for sunlight photocatalytic degradation of MO over P25 and Co–Ti–O(T-0.24) catalysts. One can see that the MO concentration decreases over all catalysts for an illumination time of 1 day. By prolonging the illumination time up to 4 days, the rate of decrease in the MO concentration becomes smaller over P25, but remains large enough over Co–Ti–O(T-0.24). For an illumination time longer than 4 days, the MO concentration decreases only slightly over all catalysts. The activity of photocatalytic degradation of MO occurs in the sequence Co–Ti(923-0.24) > CoTi(773-0.24) > Co–Ti(1023-0.24) > P25 > Co–Ti(1123-0.24). For an illumination time of 6 days, the MO concentration decreases

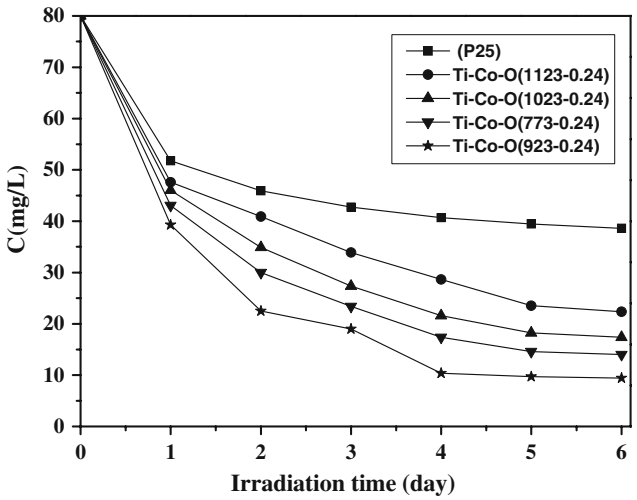

Fig. 16 Kinetic of the sunlight photo degradation of MO aqueous solutions over P25 and Co–Ti–O(T-0.24)

from the original 80 mg/L to 9.43, 14.02, 17.38, 22.34 and 38.63, corresponding to a MO conversion of 88.21, 82.48, 78.27, 72.07 and 51.71%, over Co–Ti(923-0.24), CoTi(773-0.24), Co–Ti(1023-0.24), P25 and Co–Ti(1123-0.24), respectively.

3.3 The Active Phase and Active Site Over the Replicated Mesoporous Co–Ti Oxides

The results regarding the photo degradation of MO indicate that both the Co/Ti atomic ratio and calcination temperature affect the photocatalytic activity of the Co–Ti(T–R) catalysts. For Co–Ti(773-R) catalysts, the photocatalytic activities are higher than for the pure titania and increase with the Co/Ti atomic ratio. For the Co–Ti(T-0.24) catalysts, the photocatalytic activities exhibit the sequence Co–Ti(923-0.24) > CoTi(773-0.24) > Co–Ti(1023-0.24) > P25 > Co–Ti(1123-0.24).

The results of XRD, N_2-physisorption and TEM show that, for Co–Ti(773-R), the crystal size and specific surface area decrease, the mesopore size increases, and the crystalline phase transforms from a mixture of anatase and rutile into anatase, with increasing Co/Ti atomic ratio. For Co–Ti(T-0.24), the crystal size and mesopore size increase, the specific surface area decreases, and the crystalline phase transforms from anatase first into a mixture of anatase with a higher Co/Ti atomic ratio and rutile and finally into a mixture of rutile and $CoTiO_3$, with increasing calcination temperature. From the above results, one can conclude that the specific surface area and crystal size are probably not the predominant factors that affect the photocatalytic performance of the replicated mesoporous Co–Ti oxide, even though titania with a larger specific surface area and/or smaller average crystal size is usually much more active in photocatalysis than that with a smaller specific surface area and/or a larger average crystal size [52, 53]. We consider that the anatase phase with a larger pore size, which is favorable to mass transfer, and a higher Co/Ti atomic ratio, which introduces more active sites, contribute to the high photocatalytic performance of the replicated mesoporous Co–Ti oxide catalyst.

The UV/Vis-DRS characterization reveals that in the UV light range, Co–Ti(773-R) and Co–Ti(T-0.24) exhibit higher absorptions than pure titania, with their band edges extended into the range of visible light absorption. Comparing to the pure titania, Co–Ti(T-0.24) catalysts display blue-shifts of the UV adsorptions. An exception is that the UV absorption is lower and has no blue-shift over Co–Ti–O(1123-0.24). The high absorption can be ascribed to the incorporation of Co^{2+} ions into the lattice of anatase, which generate more sites for the C–T ($O^{2-} \rightarrow Ti^{4+}$) transition. The blue shift is due to the formation of Co^{3+} and Ti^{3+} and this C–T transition requires a higher energy.

Both the high absorption and the blue shift in the range of the UV light are responsible for the high photocatalytic activity of a photo catalyst [54], consistent with the UV light photocatalytic degradation of MO in this work. In the sunlight range, the absorptions, caused by the d-electron transitions of Co^{2+} and Co^{3+} ions as well as the interband transition of Co^{2+} to Ti^{4+} ions, have been identified over Co–Ti–O(T–R), in contrast to their absence over pure titania. These absorptions cause the higher activity of the sunlight degradation of MO over Co–Ti–O(T–R) than over pure titania. In addition, the absorption bands of Co^{3+} ions disappear and those of Co^{2+} are enhanced over Co–Ti(1023-0.24) and Co–Ti(1123-0.24) catalysts, compared to Co–Ti(773-0.24) and Co–Ti(923-0.24), due to the transformation of cobalt-containing anatase into rutile and $CoTiO_3$ phases at high calcination temperatures. This suggests that the Co^{3+} ions are responsible for the high photocatalytic activity of Co–Ti–O(T–R). From the above discussion, one can conclude that the active sites of the replicated mesoporous Co–Ti oxide catalysts may be a result of the incorporation of the Co^{2+} into the framework of the anatase phase, and especially, of the formation of Co^{3+} ions due to the electron transfer from the Co^{2+} to the Ti^{4+} ions.

4 Conclusion

Mesoporous Co–Ti oxides have been synthesized via the nano-replication route. The obtained materials possess a nanospherical morphology and a mesoporous structure, with the walls of the mesopores composed mainly of cobalt-incorporated anatase. The Co^{3+} ions are formed in the replicated mesoporous Co–Ti oxides, via the transfer of electrons from Co^{2+} to Ti^{4+} ions. The replicated mesoporous Co–Ti oxides exhibit higher activities in the photocatalytic degradation of methyl orange than pure titania. Besides the higher diffusion, the cobalt-containing anatase, as the active phase, and the Co^{3+} ions, as the active sites, contribute to the high photocatalytic activities of the replicated mesoporous Co–Ti oxides.

Acknowledgment We are grateful to the financial support from the Program for New Century Excellent Talents in University, the Ministry of Education of P. R. China; and the Program for Lotus Scholar in Hunan Province, P. R. China.

References

1. Chuah GK, Hu X, Zhan P, Jaenicke S (2002) J Mol Catal A: Chem 181:25–31
2. Sage V, Clark JH, Macquarrie DJ (2003) J Mol Catal A: Chem 198:349–358
3. Kalogeras IM, Vassilikou-Dova A, Neagu ER (2001) Mater Res Innov 4:322–333
4. Matthias G, Wark M, Wörle D, Schulz-Ekloff G (2000) Angew Chem 112:167–170
5. Pan A, Zheng H, Yang Z, Liu F, Ding Z, Qian Y (2003) Mater Res Bull 38:789–796
6. Coradin T, Larionova J, Smith AA, Rogez G, Cléac R, Guéin C, Blondin G, Winpenny REP, Sanchez C, Mallah T (2002) Adv Mater 14:896–898
7. Kresge CT, Leonowicz ME, Roth WJ, Vartuli JC, Beck JS (1992) Nature 359:710–712
8. Beck JS, Vartuli JC, Roth WJ, Leonowicz ME, Kresge CT, Schmitt KD, Chu CTW, Olson DH, Sheppard EW et al (1992) J Am Chem Soc 114:10834–10843
9. Ciesla U, Schueth F (1999) Microporous Mesoporous Mater 27:131–149
10. Corma A, Kumar D (1998) In Mesoporous molecular sieves 1998, vol 117. Elsevier Science Publ B V, Amsterdam, pp 201–222
11. Taguchi A, Schuth F (2005) Microporous Mesoporous Mater 77:1–45
12. Zhao D, Feng J, Huo Q, Melosh N, Fredrickson GH, Chmelka BF, Stucky GD (1998) Science 279:548–552
13. Huo Q, Margolese DI, Clesla U, Feng P, Gler TE, Sieger P, Leon R, Petroff PM, Schuth F, Stucky GD (1994) Nature 368:317–321
14. Tanev PT, Pinnavaia TJ (1995) Science 267:865–867
15. Bagshaw SA, Prouzet E, Pinnavaia TJ (1995) Science 269:1242
16. Tanev PT, Chibwe M, Pinnavaia TJ (1994) Nature 368:321–323
17. Antonelli DM, Ying JY (1995) Angew Chem (International Edition in English) 34:2014–2017
18. Antonelli DM, Nakahira A, Ying JY (1996) Inorg Chem 35:3126
19. Tian Z-R, Tong W, Wang J-Y, Duan N-G, Krishnan VV, Suib SL (1997) Science 276:926–930
20. Srivastava DN, Perkas N, Gedanken A, Felner I (2002) J Phys Chem B 106:1878–1883
21. Yuan M, Shan Z, Tian B, Tu B, Yang P, Zhao D (2005) Microporous Mesoporous Mater 78:37–41
22. Shyue JJ, DeGuire MR (2005) J Am Chem Soc 127:12736–12742
23. Perkas N, Palchik O, Brukental I, Nowik I, Gofer Y, Koltypin Y, Gedanken A (2003) J Phys Chem B 107:8772–8778
24. Liu Z, Zhang J, Han B, Du J, Mu T, Wang Y, Sun Z (2005) Microporous Mesoporous Mater 81:169–174
25. Ruckenstein E, Chao ZS (2001) Nano Lett 1:739–742
26. Wu G, Wang X, Chen B, Li J, Zhao N, Wei W, Sun Y (2007) Appl Catal A: Gen 329:106–111
27. Kruk M, Jaroniec M, Ryoo R, Joo SH (2000) J Phys Chem B 104:7960–7968
28. Hashimoto K, Wasada K, Osaki M, Shono E, Adachi K, Toukai N, Kominami H, Kera Y (2001) Appl Catal B: Environ 30:429–436
29. Buciuman FC, Patcas F, Hahn T (1999) Chem Eng Process 38:563–569
30. Chen H, Sayari A, Adnot A, Larachi F (2001) Appl Catal B: Environ 32:195–204
31. Bessell S (1993) Appl Catal A: Gen 96:253–268
32. Hoffmann MR, Martin ST, Choi W, Bahnemann DW (1995) Chem Rev 95:69–96
33. Yang Q, Choi H, Dionysiou DD (2007) Appl Catal B: Environ 74:170–178
34. Gracien EB, Shen J, Sun X, Liu D, Li M, Yao S, Sun J (2007) Thin Solid Films 515:5287–5297
35. Kazachkov SG, Chashechnikova IT, Vorotyntsev VM, Golodets GI (1989) Petrol Chem USSR 29:123–129
36. Sun C, Tao L, Liang H, Huang C, Zhai H, Chao Z (2006) Mater Lett 60:2115–2118
37. Ryoo R, Joo SH, Jun S (1999) J Phys Chem B 103(37):7743–7746

38. Wang Y, Chen S, Tang X, Palchik O, Zaban A, Koltypin Y, Gedanken A (2001) J Mater Chem 11:521–526
39. Wang Y, Tang X, Yin L, Huang W, Hacohen YR, Gedanken A (2000) Adv Mater 12:1183–1186
40. Barrett EP, Joyner LG, Halenda PP (1951) J Am Chem Soc 73:373–380
41. Sing KSW, Everett DH, Haul RAW, Moscou L, Pierotti RA, Rouqerol J, Siemieniewska T (1985) Pure Appl Chem 57:603–619
42. Kruk M, Jaroniec M (2001) Chem Mater 13:3169–3183
43. Brik Y, Kacimi M, Ziyad M, Bozon-Verduraz F (2001) J Catal 202:118–128
44. Anpo M, Takeuchi M (2003) J Catal 216:505–516
45. Anpo M (2004) Bull Chem Soc Japan 77:1427–1442
46. Iketani K, Sun R-D, Toki M, Hirota K, Yamaguchi O (2004) Mater Sci Eng B: Solid-State Mater Adv Technol 108:187–193
47. Martin ST, Morrison CL, Hoffmann MR (1994) J Phys Chem 98:13695–13704
48. Sathish M, Viswanathan B, Viswanath RP, Gopinath CS (2005) Chem Mater 17:6349–6353
49. Vorontsov AV, Dubovitskaya VP (2004) J Catal 221:102–109
50. Wu JCS, Chen C (2004) J Photochem Photobiol A: Chem 163:509–515
51. Nozik AJ (1993) In: Ollis DF, Al-Ekabi H (eds) Photocatalytic purification and treatment of water and Air [M]. Elsevier, Amsterdam, p 391
52. Martin ST, Herrmann H, Choi WY, Hoffmann MR (1994) Faraday Trans 90:3315–3323
53. Lever ABP (1984) Inorganic electronic spectra. Elsevier, Amsterdam, p 480
54. Lin J, Yu JC, Lo D, Lam SK (1999) J Catal 183:368–372